BASIC SCIENCES

Physical Contacts Between Mitochondria and WPBs Participate in WPB Maturation

Jing Ma,* Zhenhua Hao,* Yudong Zhang, Liuju Li, Xiaoshuai Huang, Yu Wang, Liangyi Chen, Ge Yang, Wei Li

BACKGROUND: Weibel-Palade bodies (WPBs) are endothelial cell–specific cigar-shaped secretory organelles containing various biologically active molecules. WPBs play crucial roles in thrombosis, hemostasis, angiogenesis, and inflammation. The main content of WPBs is the procoagulant protein vWF (von Willebrand factor). Physical contacts and functional cross talk between mitochondria and other organelles have been demonstrated. Whether an interorganellar connection exists between mitochondria and WPBs is unknown.

METHODS: We observed physical contacts between mitochondria and WPBs in human umbilical vein endothelial cells by electron microscopy and living cell confocal microscopy. We developed an artificial intelligence–assisted method to quantify the duration and length of organelle contact sites in live cells.

RESULTS: We found there existed physical contacts between mitochondria and WPBs. Disruption of mitochondrial function affected the morphology of WPBs. Furthermore, we found that Rab3b, a small GTPase on the WPBs, was enriched at the mitochondrion-WPB contact sites. Rab3b deficiency reduced interaction between the two organelles and impaired the maturation of WPBs and vWF multimer secretion.

CONCLUSIONS: Our results reveal that Rab3b plays a crucial role in mediating the mitochondrion-WPB contacts, and that mitochondrion-WPB coupling is critical for the maturation of WPBs in vascular endothelial cells.

GRAPHIC ABSTRACT: A graphic abstract is available for this article.

Key Words: endothelial cells ■ mitochondrion ■ organelle interaction ■ von Willebrand factor ■ Weibel-Palade body

Weibel-Palade bodies (WPBs) are specialized secretory organelles in vascular endothelial cells. As a member of lysosome-related organelles,[1–3] WPBs store vWF (von Willebrand factor), t-PA (tissue-type plasminogen activator), P-selectin, IL8 (interleukin-8), angiopoietin-2, and ions such as H^+ and Ca^{2+}.[4–8] Upon stimulation, these contents are quickly released to participate in coagulation, angiogenesis, inflammation, and thrombosis.[9] Abnormalities in the biogenesis or secretion of WPBs can lead to various diseases such as coagulation disorders and thrombosis. For example, a deficiency or reduction in vWF levels in the blood causes von Willebrand disease,[10] while high level of vWF in the blood leads to thrombotic thrombocytopenic purpura.[11]

Studies have also shown that vWF is directly related to atherosclerosis.[12] The main component of WPBs is vWF, which assembles into tubular structures observed under electron microscopy.[13]

The remarkable cigar shape of WPB is because of the tubule architecture of vWF.[9] vWF is synthesized as a proprotein and dimerized in the endoplasmic reticulum. In the acidic milieu of the Golgi apparatus, vWF undergoes proteolytic cleavage, self-assembly, and tubulation.[5,14] vWF forms nanoclusters of about 0.5 μm in length in the mini-stacks of the Golgi apparatus and then packages into nascent WPBs at the trans-Golgi network.[15] After budding from the TGN (trans-Golgi network), immature WPBs with low electron density and irregular tubular

Nonstandard Abbreviations and Acronyms

AP-3	adaptor protein complex-3
BLOC-2	biogenesis of lysosome-related organelles complex-2
HUVEC	human umbilical vein endothelial cell
IL8	interleukin-8
NC	negative control
PMA	phorbol-12-myristate-13-acetate
SIM	structured illumination microscopy
t-PA	tissue-type plasminogen activator
vWF	von Willebrand factor
WPB	Weibel-Palade body

Highlights

- We demonstrated the physical contacts between Weibel-Palade bodies and mitochondria.
- Disruption of mitochondrial function affected the morphology of Weibel-Palade bodies.
- Knocking down of *RAB3B* reduced the contacts between Weibel-Palade bodies and mitochondria, thereby compromising Weibel-Palade body elongation and maturation.

structure localize at the perinuclear region.[16] During maturation, excessive membrane components are removed, the contents are concentrated, and the lumen is acidified.[17–20] Mature WPBs with high electron density and regular arrangement of inner tubular structures move toward the cell periphery to be secreted upon stimulation. vWF undergoes constitutive secretion, basal secretion, and regulated secretion from vascular endothelial cells. vWF multimers are secreted mainly from WPBs via regulated secretion.[4,7]

The biogenesis of WPBs is similar to other lysosome-related organelles, with the recruitment and transport of contents and membrane components regulated by the endo-lysosomal transport system. Some components such as t-PA, angiopoietin-2, osteoprotegerin, and P-selectin are recruited with vWF during budding from TGN, while others such as CD63, Rab27a, RalA, and Rab3d are transported into WPBs after detachment from TGN. For example, the AP-3 (adaptor protein complex-3) transports CD63 to WPBs.[21] Several molecules involved in WPB maturation and exocytosis have been identified. The BLOC-2 (biogenesis of lysosome-related organelles complex-2) subunit HPS6 (Hermansky-Pudlak syndrome 6) is involved in the transport of V-ATPase subunits V0D1 and V0A1 to WPBs, which is crucial for WPB acidification and regulated vWF secretion.[17,22,23] Rab27a and its effector protein MyRIP, which binds myosin VIIa and Va, play a role in WPB localization to the actin cytoskeleton, preventing incomplete WPBs from releasing their contents.[24]

The mitochondrion is a highly dynamic organelle that constantly reorganizes its structure and interacts with other organelles through membrane contacts. It has been proved that mitochondria have physical contact with various organelles, including the endoplasmic reticulum,[25] lipid droplets,[26] lysosomes,[27] and melanosomes.[28] Such interactions have been associated with many pivotal functions, such as organelle biogenesis,[28] calcium homeostasis,[25] lipid metabolism,[26] and organelle homeostasis.[27] Wong et al[27] discovered an interaction between mitochondria and lysosomes, which regulates the hydrolysis of lysosomal Rab7 GTP, thereby regulating mitochondrial fission. Recent studies have suggested that there exist interactions between mitochondria and certain lysosome-related organelles, providing new insights into the biogenesis and function of lysosome-related organelles. Daniele et al[28] found that there is a physical and functional interaction between mitochondria and melanosomes, which is involved in the biogenesis of melanosomes. Our previous study also showed that there exists a communication of substances such as Ca^{2+} between mitochondria and melanosomes.[29] However, it is unclear whether mitochondria interact with WPBs.

In this study, we observed direct physical contacts between mitochondria and WPBs. We characterized the intense cross talk between the two organelles and the effects on each other by time lapse living cell confocal microscopy. We found that Rab3b, a small GTPase on the WPBs, may function in the maintenance of contacts between the two organelles. Furthermore, we first described the reduction of mitochondrion-WPB contacts by knocking down *RAB3B*-affected WPB maturation and vWF multimer secretion. Our study provides evidence of morphological and functional connections between mitochondria and WPBs.

MATERIALS AND METHODS

The data that support the findings of this study are available from the corresponding author upon reasonable request.

Antibodies

Antibodies used in immunofluorescence: mouse monoclonal anti-vWF antibodies (ab201336, 1:500, Abcam, Cambridge, United Kingdom), rabbit polyclonal anti-TOMM20 antibody (PA5-52843, 1:500, Invitrogen, Carlsbad, CA). Alexa-Fluor conjugated (488, 594, 647) secondary antibodies were from Invitrogen (A32723, A32740, A32728, 1:2000). Mouse monoclonal anti-Rab3b antibody (LS-B14533, 1:500, LSBio, Seattle, WA), mouse monoclonal anti-β-actin antibody (MA5-15739, 1:40000, Invitrogen). HRP-conjugated antimouse secondary antibodies were from ZSGB-BIO (ZB-2305, 1:5000, Beijing, China).

Plasmids

Human *RAB3B* cDNA (NM_002867) was constructed to the pEGFP-C2 by *Xho* I and *Bam*H I. vWF-GFP was a gift from Prof Voorberg J (the Netherlands). Mito-DsRed, which contains the mitochondrial localization signal of Cox8a (amino acids 1–25) on the pDsRed1-N1 (Clontech Laboratories) vector, was prepared by a former laboratory member, Dr Chang Zhang.

Cell Culture, Transfection, and Drug Treatments

Human umbilical vein endothelial cells (HUVECs) were cultured in endothelial cell growth medium-2 medium (CC-3162, Lonza, Walkersville, MD) at 37 °C in a 5% CO_2 incubator. Cells were transfected with 0.5 μg of each plasmid DNA per well of 24-well plates by using a Lipofectamine 3000 (L3000-015, Invitrogen) kit according to the manufacturer's instructions. Forty-eight hours after transfection, cells were used for live-cell imaging or immunofluorescence. For drug treatments, phorbol-12-myristate-13-acetate (PMA, P1585, Sigma-Aldrich, St. Louis, MO) was added into the endothelial cell growth medium-2 medium with 80 nmol/L final concentration and incubated for 30 minutes at 37 °C.[22] Then cells were washed 2× with a growth medium and returned to the fresh growth medium for the indicated time. Carbonyl cyanide 3-chlorophenyl-hydrazone (C2759-100MG, Sigma-Aldrich) or oligomycin A (S1478, Selleck, Houston, TX) was added in the growth medium at a final concentration of 5.5 or 1.2 μM respectively, and cells were incubated for the indicated time at 37 °C.[29]

RNA Interference

Cells were transfected with Lipofectamine RNAiMAX transfection reagent (13778 to 500, Invitrogen) according to the manufacturer's instructions. Cells were treated with 120 nmol/L siRNAs and fixed with 4% paraformaldehyde (P6148, Sigma-Aldrich) or lysed with cell lysis buffer 72 hours after transfection. siRNA sequences targeting indicated human genes were synthesized in GenePharma (Shanghai, China), as shown in Table S1.

Immunofluorescence

Cells plated on coverslips were fixed with 4% paraformaldehyde for 20 minutes and permeabilized with 0.4% Triton X-100 (V900502, Sigma-Aldrich) in PBS (8 g NaCl, 3.58 g $Na_2HPO_4H_2O$, 0.2 g KCl, 0.24 g KH_2PO_4 dissolved in ultra-pure H_2O with final volume 1 L) for 15 minutes at room temperature. Fixed cells were blocked for 2 hours with 1% BSA in PBS and incubated with indicated primary antibodies in PBS containing 1% BSA overnight at 4 °C and then with Alexa-Fluor-conjugated secondary antibodies for 1 hour at room temperature. Coverslips were mounted with fluorescent mounting medium with or without DAPI (ZLI-9557 or ZLI-9556, ZSGB-BIO).

Confocal Microscopy

Confocal images were acquired on a Zeiss LSM 980 laser-scanning confocal microscopy equipped with 405, 488, 561, and 647 nm excitation lasers and Airyscan 2 module. Images were taken with a 100×1.4 NA oil objective (Zeiss, Oberkochen, Germany) using ZEN-Blue. For WPB size and number measurement, images of immuno-stained cells were collected for each channel with a zoom factor of 0.6 using the Airyscan 2 super-resolution acquisition mode. For live-cell imaging acquisition, a 35 mm glass-bottom dish (81158, Zeiss) with living cells was placed in a 37 °C live-cell chamber with 5% CO_2. Image series were obtained using the Airyscan 2 super-resolution acquisition mode at 666×666 pixels, 3× magnification.

Structured Illumination Microscopy

Three-dimensional-structured illumination microscopy (SIM) images of immunofluorescently stained cells were acquired on a DeltaVision OMX V4 imaging system (GE Healthcare) with a 63×1.4 oil objective (Olympus UPlanSApo), solid-state multi-mode lasers (405, 488, and 561 nm), and an sCOMS camera (PCO edge, Germany). For Hessian-SIM microscopy, HUVECs were plated on coverslips, and fixed cells were double-stained with vWF and cyto C. Images were collected and analyzed as described.[30] Briefly, Hessian-SIM microscopy was set up on a microscopy (IX83, Olympus, Japan) equipped with 488 and 561 nm excitation lasers (Sapphire 488LP-200 and Sapphire 561LP-200, Coherent, CA) and a sCMOS camera (Flash 4.0 V2, Hamamatsu, Japan). Images were taken by 2D-SIM mode with an Apo N 100X/1.7 HI oil objective (Olympus) using HCImage. The reconstruction of the images was processed using MATLAB software.

Immunoelectron Microscopy

A volume of a fixative of 4% wt/vol paraformaldehyde (PFA)+0.4% wt/vol glutaraldehyde in 0.1M PB buffer (95 mL 0.2M $NaH_2PO_4.2H_2O$ was mixed with 405 mL 0.2M $Na_2HPO_4.12H_2O$, and the volume was supplemented to 1 L with ultra-pure water; pH, 7.4) equal to the medium volume was added to living HUVEC cells. Cells were incubated in the medium-fixative mixture for 15 minutes at room temperature and continued fixed with fresh 2% wt/vol PFA+0.2% wt/vol GA in PB (pH 7.4) for 1 hour. Cells were collected and suspended in 12% wt/vol gelatin (147116.1210, PanReac/AppliChem, Germany) in PBS at 37 °C for 15 minutes. Samples were subsequently incubated on ice to solidify the gelatin and were cut into small blocks. Blocks were placed in 2.3M sucrose (dissolved in 0.1M PB buffer) overnight at 4 °C and later removed to aluminum specimen holders and transferred to liquid nitrogen. Ultrathin sections (80-nm thick) were cut using a cryo-ultramicrotome (EM FC7, Leica, Germany) and transferred to grids. Grids were washed 3× for 15 minutes with PB, 2× for 10 minutes with 0.15% Glycine, 1% BSA for 30 minutes at room temperature, and then incubated with the rabbit polyclonal anti-vWF antibodies (A0082, 1:20, Dako, Carpinteria, CA) overnight at 4 °C and goat-anti-rabbit IgG-gold 10 nm (1:50, Aurion, Wageningen, the Netherlands) secondary antibody for 1 hour at room temperature. Labeled samples were incubated with uranyl acetate/methyl cellulose (1:9) for 5 minutes. Samples were analyzed in a transmission electron microscopy (FEI Tecnai Spirit) operating at 100 kV.

High-Pressure Freezing/Freeze Substitution

HUVEC monolayers were directly grown on a 3×0.16 mm sapphire disc. The disc was quickly capped onto a 100-μm well

carrier prefilled with 1-Hexadecene for high-pressure freezing (HPF, Compact-03, Switzerland). Samples were transferred into 2% OsO_4 in 100% acetone and then placed into a freeze-substitution device (Leica EM AFS2) with the Quick Freeze Substitution Equipment (Center for Biological Imaging, core facilities for Protein Science, IBP, CAS). The samples were held at −90 °C for 6 hours, then warmed at 10 °C per hour to −60 °C, held for 1 hour, then warmed up to −30 °C, held for 1 hour, then slowly warmed to 0 °C (10 °C/h). Following freeze substitution, samples were washed 3× (15-minute intervals) in acetone at 0 °C and one time at room temperature, then stained with 0.5% UA (uranyl acetate, in acetone) for 2 hours at room temperature and washed 4×. After that, samples were embedded with SPI-PON812 resin (SPI-Pon 812 epoxy resin monomer (02659-AB), dodecenyl succinic anhydride (02827-AF), nadic methyl anhydride (02828-AF), N, N-dimethylbenzylamine (02821), SPI supplies, West Chester, PA) and polymerized 12 hours at 45 °C, and 48 hours at 60 °C. Ultrathin sections (70-nm thick) were cut with a microtome (Leica EM UC6) and examined using a transmission electron microscope (FEI Tecnai Spirit).

Transmission Electron Microscopy and 3D Electron Tomography

HUVEC cells were seeded directly on a 3 mm×0.16 mm sapphire disc. Cells on the disc were fixed with 2.5% glutaraldehyde in 0.1M PB buffer (pH 7.4), washed 4× in 0.1M PB buffer. Then, cells were immersed in an aqueous solution containing 1% (wt/vol) OsO_4 and 1.5% (wt/vol) potassium ferricyanide and incubated at 4 °C for 40 minutes. After washing, the cells were successively incubated in 1% thiocarbohydrazide (Sigma-Aldrich) at room temperature for 10 minutes, 1% unbuffered OsO_4 aqueous solution at 4 °C for 30 minutes, and 2% UA at room temperature for 40 minutes with 4 rinses in ddH_2O for 6 minutes between each step. Samples were dehydrated through graded alcohol (30%, 50%, 70%, 80%, 90%, 100%, 100%, 5 minutes each) into pure acetone (2×, 5 minutes each). Finally, samples were embedded with SPI-PON812 resin and polymerized for 12 hours at 45 °C, then 48 hours at 60 °C.[31] The ultrathin sections (70 nm) were sectioned with microtome (EM UC6, Leica), collected on copper grids, and examined in a transmission electron microscopy (FEI Tecnai Spirit) operating at 100 kV. For electron tomography, copper grids were analyzed in a Talos F200C TEM (transmission electron microscopy; FEI) operating at 200 kV equipped with a Ceta Camera (Thermo Fisher Scientific, Waltham, MA). Mitochondrion-WPB contact was imaged at 36 000× and the tilt angle started at −45° and ended at 35° with a base increment of 2°. Automated electron microscope tomography acquisition was performed by SerialEM Version 4.0.9. After reconstruction with Aretomo 1.1.0, the organelle surfaces were rendered after manual contouring by using the Imaris 10 software.

Western Blotting

Western blotting was performed as previously described.[22] Cells were washed with PBS and homogenized in a cell lysis buffer (20 mmol/L Tris [pH 7.5], 150 mmol/L NaCl and 1% Triton X-100). A postnuclear supernatant (1000 g for 10 minutes) was boiled for 5 minutes, separated by 10% SDS-PAGE gels, and transferred to a PVDF membrane, then labeled with primary antibodies and followed by an HRP-conjugated antirabbit or antimouse secondary antibody. Signals were developed using a SuperSignal West Pico chemiluminescence (ECL) kit (NCI5080, Thermo Fisher Scientific). Membranes were cut to blot target proteins and the loading control proteins.

vWF Multimer Analysis

Cells in 24-well plates were treated with 80 nmol/L PMA in 200 μL growth medium for 1 hour, then the supernatant of each well was collected and centrifuged at 1000g for 10 minutes. vWF multimer analysis was described previously.[17] The 1.2% agarose gels were prepared by dissolving Seakem high gelling temperature agarose (50041, Lonza) in 0.375 mol/L Tris (pH 8.8) with SDS added to a final concentration of 0.1%. Supernatant samples (6 μL) were loaded in 50 mmol/L Tris pH 8.0, 1% SDS, 5% glycerol, and 0.002% bromophenol blue. Gels were run at 30 V for 16 hours (EPS600, Tanon, Shanghai, China) before transfer to a nitrocellulose membrane, labeled with rabbit anti-vWF antibody followed by an HRP-conjugated anti-rabbit secondary antibody and developed by chemiluminescence ECL kit (NCI5080, Thermo Fisher Scientific). The multimers of each lane on the same gel were arranged according to molecular weight. Multimer gels were analyzed using NIH Image J software.

Artificial Intelligence–Assisted Quantification of Contact Sites

Each acquired movie consists of two channels: one for mitochondria (MITO) and the other for WPB. For the MITO channel, individual mitochondria were segmented using a deep neural network U-Net[32] to obtain their binary masks. For the WPB channel, individual WPBs were first identified using the object detection function of the TrackMate toolkit,[33] and the total number of WPBs was determined from the number of identified objects. The final binary masks of WPBs were generated through adaptive thresholding-based segmentation. Incorrect binary masks were filtered out by taking the intersection of the TrackMate detection results and the segmentation binary masks. The length of the bounding rectangular box of each connected region detected was used as the WPB length. The boundary of each WPB was then extracted from its mask. Next, each intersection of MITO binary masks and WPB edges was marked as a contact site. The number of contact events at a specific time point was determined by counting the total number of contact sites. In the meantime, the number of WPBs with contact events was also calculated. Finally, the full trajectories of individual contact sites were acquired using TrackMate. The trajectories were then used to determine the duration of individual contact events. The overall workflow is summarized in Figure 2A.

Real-Time PCR

mRNA was prepared from negative control (NC) and knockdown HUVECs using RNeasy mini kit (74104, Qiagen, Hilden, Germany) according to the manufacturer's instructions. The isolated mRNA was then subjected to reverse transcription using the iScript cDNA synthesis kit (1708891, Bio-Rad, Hercules, CA). Real-time PCR was performed using SuperReal PreMix

Color (SYBR Green) kit (FP215-02, Tiangen, Beijing, China) in a QIAGEN Rotor-Gene Q MDx qPCR machine. The primers used for each gene were shown in Table S2. The C(T) data were normalized with an GAPDH internal control and analyzed using the 2(−ΔΔC(T)) method.[34]

Statistical Analysis

NIH Image J software and GraphPad Prism 8 software (Graphpad, La Jolla, CA) were used for statistical analysis. All data were shown as the mean±SEM. Comparisons were statistically tested using the Student t test, the ANOVA test, or the nonparametric Kruskal-Wallis test. A difference of $P<0.05$ was considered statistically significant.

RESULTS

Physical Contacts Between Mitochondria and WPBs

We first investigated whether there are physical contacts between mitochondria and WPBs. We performed high-pressure-frozen electron microscopy in HUVECs. We observed that WPBs (Figure 1A in cross-section and Figure 1B in longitudinal section) contacted with mitochondria. Moreover, a single WPB could form a long circular contact site with the mitochondrial membrane (Figure 1C). Immunoelectron microscopy images also showed physical proximity between vWF-labeled WPBs and mitochondria (Figure 1D and 1E). To highlight the membrane structure of the organelles, we implemented the electron microscopy using the reduced osmium tetroxide-thiocarbohydrazide-osmium method and quantified the proportion of WPBs with contacts. The representative figures showed the close contact between mitochondria and WPBs (Figure 1F through 1H). Quantitative results showed that the average proportion of mitochondria-interacting WPBs relative to the total WPBs was 21.9% (Figure 1I). Similarly, our electron microscopy images revealed the contacts between mitochondria and WPBs in the endothelial cells isolated from the aorta of adult mice (4 months, data not shown).

Additionally, we performed electron tomography and 3D reconstruction to illustrate the interaction sites between mitochondria and WPBs. It was clearly shown that the two organelles were in contact with each other, and the distinctive protein tethers can be observed (Figure 1J through 1L; Video S1). Taken together, WPBs are capable of forming physical contacts with mitochondria.

Dynamic Contact Events Between Mitochondria and WPBs in Live Cells

To investigate whether there are active interactions between mitochondria and WPBs, we next examined mitochondrion-WPB contacts in live cells, which would provide information of nonrandom association of the two organelles. HUVECs were transfected with a WPB marker vWF-GFP and a mitochondrial marker Mito-dsRed. Images were taken by real-time confocal microscopy at the super-resolution mode. WPBs could contact multiple mitochondria simultaneously or in succession (Video S2). Contact events appeared stable as WPBs were tightly associated with mitochondria, although both organelles were highly dynamic (Video S2). We developed an algorithm to quantify the contact events. The overlapped vWF-GFP and Mito-dsRed fluorescence marked the boundary between a WPB and a mitochondrion, being likely a potential contact (Figure 2A and 2B). By quantitative analysis of the videos, 35.1% of WPBs were in contact with mitochondria (Figure 2C). The average length of the contacts accounted for 18.4% of the average WPB perimeter (Figure 2D and 2E), and 17.4% of WPBs were tightly associated with mitochondria for more than 10 seconds (see the distribution map in Figure 2F). The average duration of each contact event lasted for 5.84 seconds (n=3028). We calculated the length of the motion trajectory of the midpoint of each contact site during the detection time. The result showed that 35.5% of the contact trajectory could be >1 μm (see the distribution map in Figure 2G).

We observed that multiple WPBs kept contacting with the mitochondria over time in distinct movement types: WPBs juxtaposed close to mitochondria, one tip of WPB attached with mitochondria and WPBs crossed with mitochondria (Figure 2H through 2J). We also observed some WPBs contacted and separated quickly with mitochondria in a kiss and run mode (Figure 2K). We observed the contacts were not coincidentally occurred through microtubules (Figure S1). Overall, these interactions between WPBs and mitochondria demonstrated that WPBs maintained physical contacts with mitochondria under dynamic conditions, suggesting that the connections between the two organelles are not coincidental.

We further investigated whether mitochondrion-WPB contacts participate in WPB dynamics. We observed WPBs rushing along with stable mitochondria and keeping contact with the mitochondria (Figure 2L; Video S3). A bent rod-shaped WPB appeared to be straightened by a moving mitochondrion at the contact sites, and the mitochondrion seemed to provide the driving force (Figure 2M; Video S4). Contact and separation between two WPBs could also be found at the mitochondrion-WPB contact site (Figure 2N; Videos S5 through S7). These images revealed that WPB morphology may be regulated during the contact process with mitochondria.

Dysfunction of Mitochondria Affects the Shape of WPBs

Next, we explored the physiological functions of the interaction between mitochondria and WPBs. Due to the classic rod-shaped morphology of mature WPB,
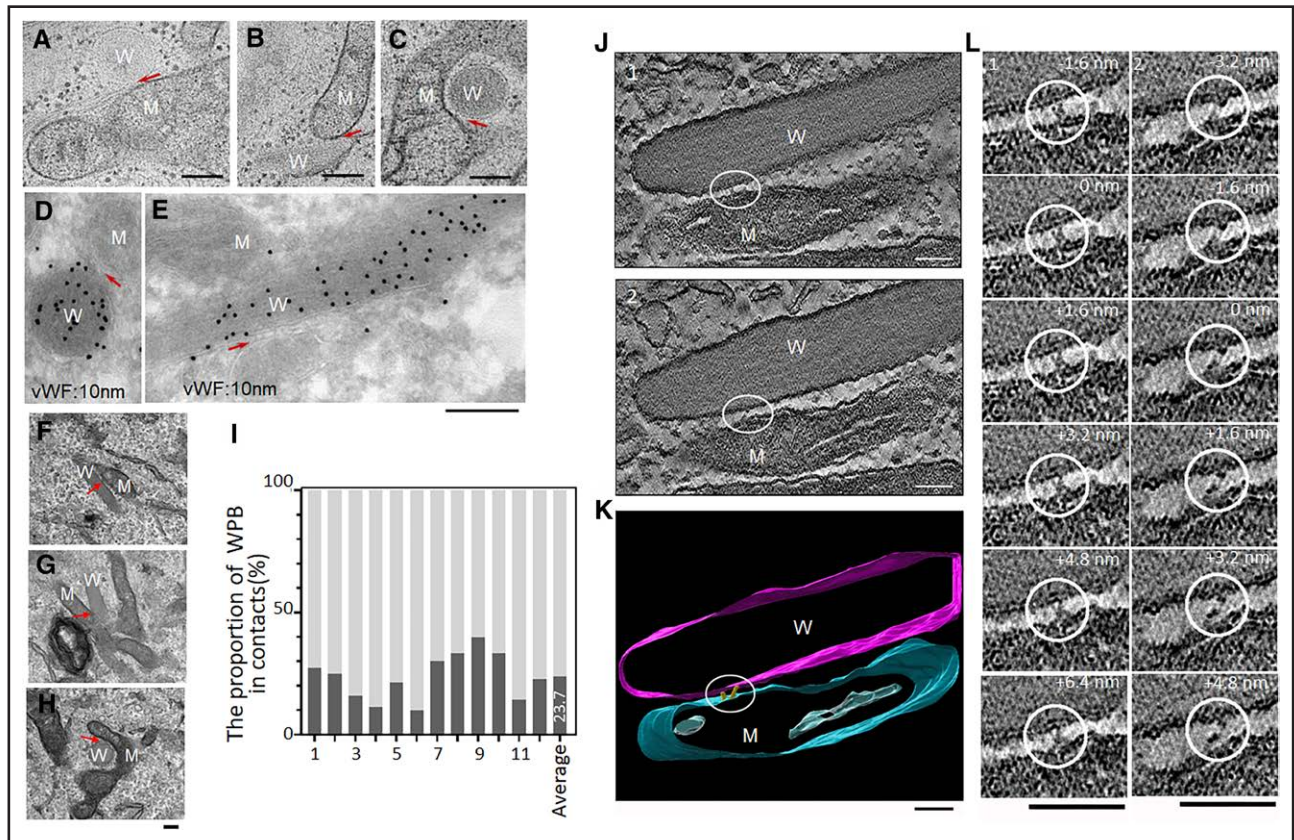
Figure 1. Contact sites between mitochondria and Weibel-Palade bodies (WPBs) in human umbilical vein endothelial cells (HUVECs).
A through **C**, Transmission EM images of high-pressure frozen HUVECs. Contact sites (red arrow) between a mitochondrion (labeled with M) and a WPB (labeled with W) are shown. Red arrows point to the contact sites. Scale bars represent 200 nm. **D** and **E**, Immunoelectron microscopy images of HUVECs. Contact sites (red arrow) between a mitochondrion and a vWF-labeled (10 nm) round WPB (**D**) or rod WPB (**E**) are shown. Scale bars represent 200 nm. **F** through **H**, Transmission EM images of HUVECs. Contact sites (red arrow) between mitochondrion and WPB are shown. Scale bars represent 200 nm. **I**, Quantification of the proportion of WPBs in contact in 12 cells. The average proportion is 23.7%. **J**, Representative slices of reconstructed electron tomography images of a contact with two protein tethers (1 and 2) between a mitochondrion and a WPB are shown. The protein tethers are shown in the circles. **K**, The 3D tomogram model of the contact in **J** shows the mitochondrial membrane (blue) and WPB membrane (purple), as well as two protein tethers (yellow). The protein tethers are shown in the circles. Please refer to Video S1 for this presentation. **L**, Sequential *z* axis enlargements of protein tethers 1 and 2. Relative position of the *z* axis on each tomogram is indicated. The protein tethers are shown in the circles. Scale bars represent 100 nm in **J** through **L**.

the abnormalities that occur in WPB biogenesis usually lead to changes in its shape, which provides a simple screening method for studying the factors that affect the biogenesis of WPB. To investigate whether the mitochondria-WPB interaction has an impact on WPB biogenesis, we first used mitochondrial inhibitors carbonyl cyanide 3-chlorophenyl-hydrazone (a potent compound for loss of mitochondrial membrane potential) and oligomycin A (an inhibitor of mitochondrial ATP synthase) to disrupt mitochondrial function in HUVEC cells, and then examined the changes of WPB morphology. Majority of vWF-labeled WPBs were rod-shaped in mock (DMSO)-treated control cells, however, the length of WPBs was significantly reduced in either carbonyl cyanide 3-chlorophenyl-hydrazone- or oligomycin A-treated cells, suggesting that mitochondrial function is critical for long rod-shape formation of WPBs (Figure 3A through 3D).

To exclude the broad effect of chemical inhibition of mitochondrial activity, we examined the effects of genetic alterations of mitochondria on WPB morphology. We disrupted mitochondrial function by knocking down several selected proteins in HUVEC cells, including those participating in mitochondrial dynamics of fusion and fission (MFN2[35] and FIS1[36]), ATP synthesis (NDUFS1, SLC25A4, SLC25A5),[37–39] mitochondrial calcium ion release (SLC8A3,[40,41] SLC8B1[42]). We used the cocktail of 3 siRNAs for each gene (Table S1). We labeled WPBs with vWF and observed that after knocking down of *MFN2, FIS1, NDUFS1, SLC25A4, SLC25A5, SLC8A3,* or *SLC8B1* (Figure 3E through 3M). Except for *SLC8B1*, the mean length of WPBs was significantly reduced compared with the NC after knockdown of these individual genes (Figure 3N). These results imply that disrupting the function of mitochondria might affect the morphology of WPB.
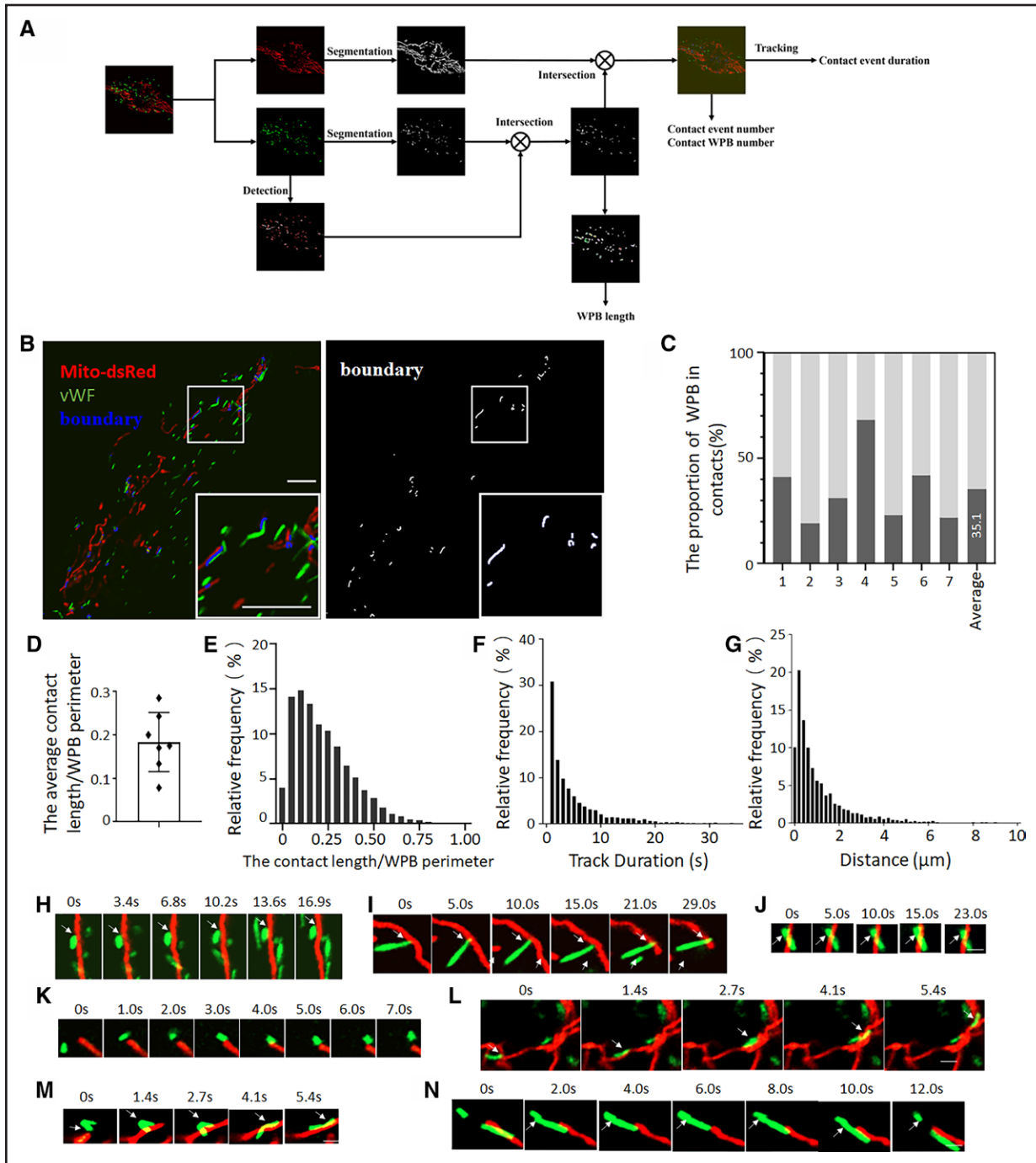
Figure 2. Contact sites between mitochondria and Weibel-Palade bodies (WPBs) in living cells.
A, An overall workflow for artificial intelligence–assisted quantification of contact sites. Contact sites at each time point were determined from intersection between segmented mitochondria and WPBs. Individual contact sites were then tracked so that their dynamic behavior including duration could be determined. **B**, Representative time-lapse super-resolution images of mitochondrion-WPB contacts in living HUVECs expressing Mito-dsRed (mitochondria, red) and vWF (von Willebrand factor)-GFP (WPBs, green). Note that boundaries between mitochondria and WPBs are recognized and labeled by blue lines in left, which are identical to white lines in right panel. Scale bars, 5 μm. **C**, Quantification of the proportion of WPBs in contact from 7 cells. The mean value is 35.1%. Three independent experiments were performed. **D**, Quantification of average ratio of mitochondria-WPB contact length to WPB perimeter per cell (n=7 cells). **E**, The distribution of average ration of mitochondria-WPB contact length to WPB perimeter (n=17270 events from 7 cells). **F**, Quantification of duration of the mitochondria-WPB contact events (n=3028 events from 7 cells). **G**, The length distribution of the motion trajectory of the midpoint of each contact (n=3028 events from 7 cells). **H** through **K**, Representative pictures of a WPB in contact with a mitochondrion (**H**), one tip of a rod-shaped WPB stably contacting a mitochondrion (**I**), a rod-shaped WPB stably crossing over a mitochondrion (**J**), and a WPB contacting a mitochondrion transiently (**K**). White arrows point to the contacting site. **L** through **N**, Representative pictures of WPB dynamics at the mitochondrion-WPB contact sites. White arrows show a WPB moving along a mitochondrion (**L**), a WPB deformation by a mitochondrion (**M**), one WPB contacting with another WPB that interacted with a mitochondrion (**N**). Please refer to the Videos S2 through S7 for the dynamics of the abovementioned events.
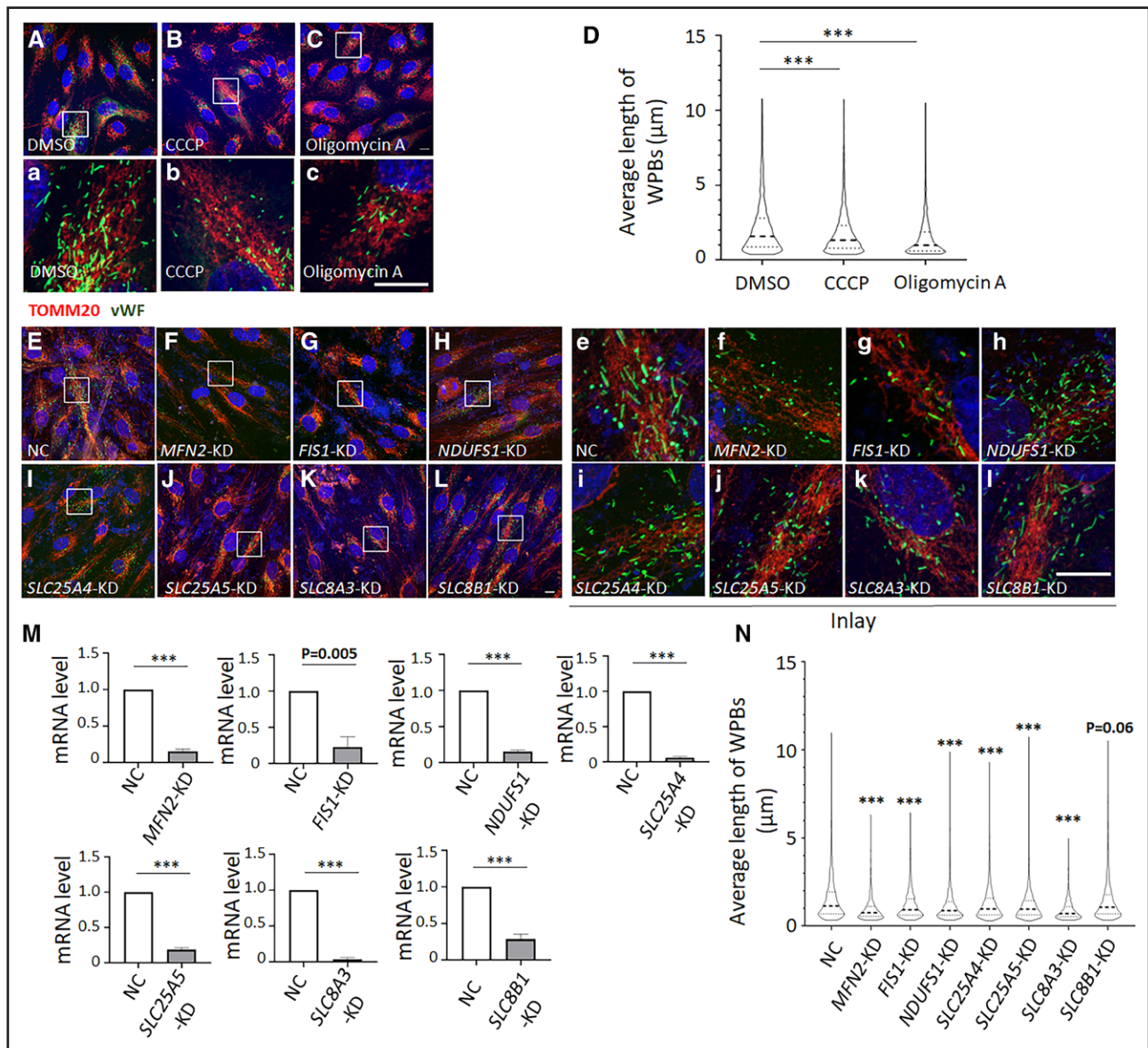
Figure 3. Dysfunctional mitochondria affect the morphology of Weibel-Palade bodies (WPBs).
A through **C**, Representative super-resolution images show that CCCP or oligomycin A treatment affects morphology of WPBs. Human umbilical vein endothelial cells (HUVECs) were treated with 5.5-μM CCCP or 1.2-μM oligomycin A in growth medium for 48 h. Equal volume of DMSO was added as a control. Then fixed cells were stained with an endogenous mitochondrial marker TOMM20 (red) and a WPB marker vWF (green). **a** through **c**, The magnified regions of the boxed areas in **A** through **C**. Scale bars, 10 μm. **D**, Quantification of length of WPBs after CCCP or oligomycin A treatment. Three independent experiments were performed. Two thousand four hundred forty-eight WPBs from DMSO-treated HUVEC cells, 1929 WPBs from CCCP-treated cells, and 2047 WPBs from oligomycin A–treated cells were analyzed. Data shown are mean±SEM, ***$P<0.001$, each treatment group was compared with the control group by nonparametric Kruskal-Wallis test with Dunn post hoc. **E** through **L**, Indicated mitochondrial genes (3 mixed siRNAs were used for each gene) were knocked down in HUVECs, fixed cells were stained with an endogenous WPB marker vWF (green) and a mitochondrial marker TOMM20 (red). Representative super-resolution images show the morphology of WPBs in control (NC) and knockdown HUVECs. **e** through **l**, The magnified regions of the boxed areas in **E** through **L**. Blue: DAPI. Scale bars, 10 μm. **M**, Reduced mRNA levels in indicated mitochondrial gene knockdown HUVECs. The mRNA level of control cells was normalized to 1. Three independent experiments were performed. Data shown are mean±SEM, n=3, ***$P<0.001$ by 2-tailed t test. **N**, Quantification of length of WPBs after knocking down the indicated mitochondrial genes. Three independent experiments were performed. Data shown are mean±SEM. WPB numbers in different cells: NC, 1843; *MFN2*-KD, 1573; *FIS1*-KD, 1591; *NDUFS1*-KD, 2019; *SLC25A4*-KD, 2433; *SLC25A5*-KD, 2452; *SLC8A3*-KD, 1191; *SLC8B1*-KD, 2825. ***$P<0.001$, each knockdown group was compared with the control group by nonparametric Kruskal-Wallis test with Dunn post hoc.

Rab3b Deficiency Leads to Abnormal WPB Shape in HUVEC Cells and Affects the Maturation of WPBs

We further explored the molecules involved in the interaction between mitochondria and WPBs. The activity of Rab GTPases is crucial for inter-organellar connections.[27,43] Therefore, we examined whether Rab proteins play a role in establishing mitochondrion-WPB contacts. Zografou et al[44] exogenously expressed 41 known Rab proteins in HUVECs, and found that Rab3a, Rab3b,

Rab3d, Rab15, Rab27a, Rab27b, Rab33a, and Rab37 are located explicitly in WPBs. These 8 Rabs are endogenously expressed in HUVECs. As the mitochondrion-WPB contact affected the morphology of WPBs, we used WPB length to screen which Rab protein is involved in mitochondrion-WPB contact. We used the cocktail of 3 siRNAs for each gene (Table S1). Our results showed that in *RAB3A, RAB3B, RAB3D, RAB15, RAB27A, RAB27B,* or *RAB37* knockdown cells, the mean length of WPBs was significantly reduced compared with control cells (Figure 4).

The phenotype of Rab3b deficiency was more profound (Figure 4K). To verify the results of mixed targets in the above screening, we knocked down HUVECs with 3 different targets of *RAB3B*, respectively, and found that all 3 targets of *RAB3B* resulted in the shortening of WPBs (Figure 5A through 5C). We further analyzed the length distribution of WPBs in *RAB3B* (target-299) knockdown cells and observed fewer long-shaped WPBs than those in control cells. There were more WPBs distributed <1.8 μm in the *RAB3B* knockdown group (Figure 5D),
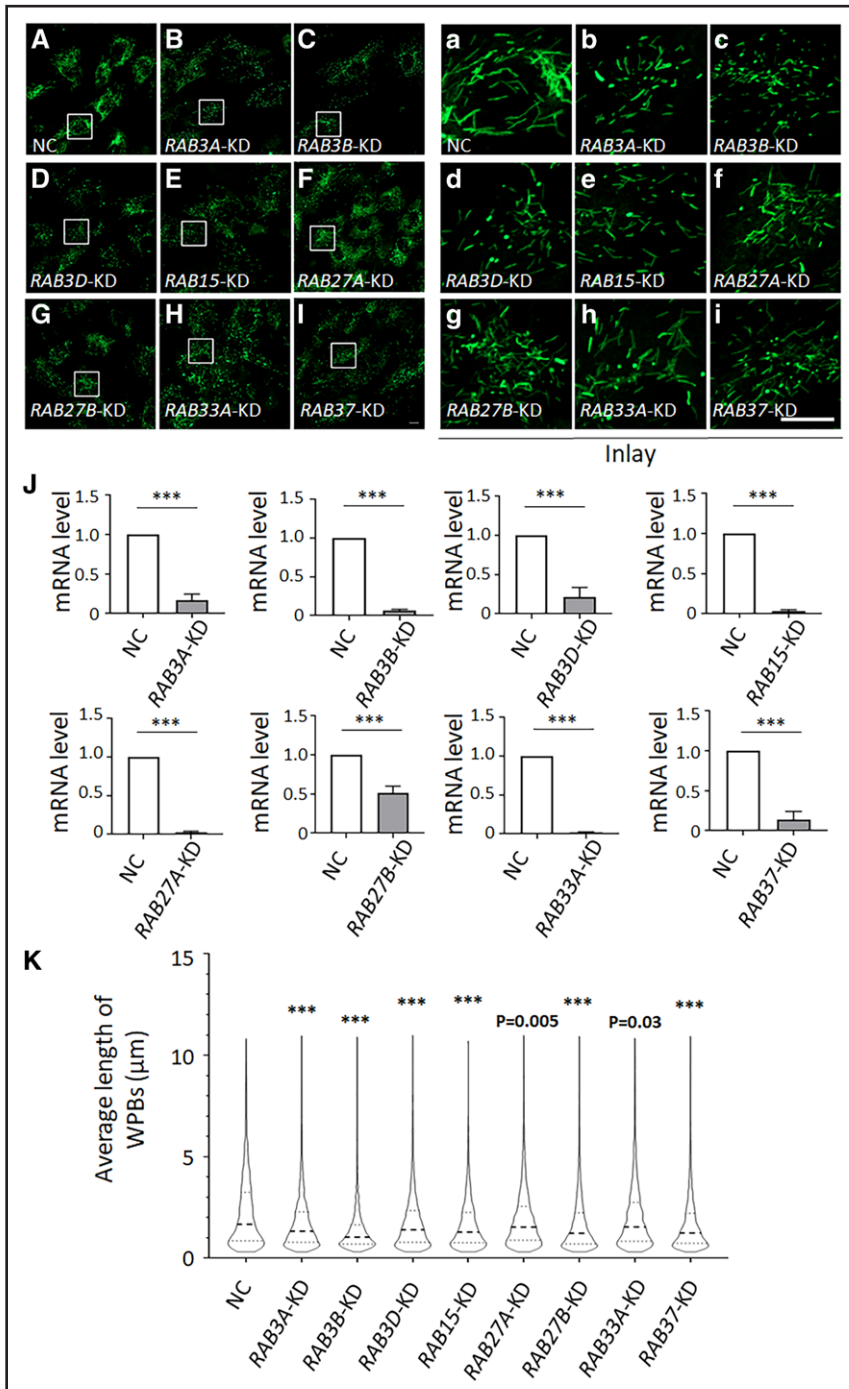

Figure 4. The average length of Weibel-Palade bodies (WPBs) is mostly reduced in *RAB3B* knockdown human umbilical vein endothelial cells (HUVECs).
A through **I**, Indicated *RAB* genes (3 mixed siRNAs were used for each gene) were knocked down in HUVECs and fixed cells were stained with an endogenous WPB marker vWF (green). Representative super-resolution images show the morphology of WPBs in control (NC) and knockdown HUVECs. **a** through **i**, The magnified regions of the boxed areas in **A** through **I**. Scale bars, 10 μm. **J**, Reduced mRNA levels in indicated *RAB* gene knockdown HUVECs. The mRNA level of control cells was normalized to 1. Three independent experiments were performed. Data shown are mean±SEM, n=3, ***P<0.001 by 2-tailed t test. **K**, Quantification of length of WPBs after knocking down the indicated *RAB* genes. Three independent experiments were performed. Data shown are mean±SEM. WPB numbers in different cells: NC, 1893; *RAB3A*-KD, 3288; *RAB3B*-KD, 2653; *RAB3D*-KD, 2983; *RAB15*-KD, 2967; *RAB27A*-KD, 3648; *RAB27B*-KD, 3242; *RAB33A*-KD, 3106; *RAB37*-KD, 4904. ***P<0.001, each knockdown group was compared with the control group by nonparametric Kruskal-Wallis test with Dunn post hoc.
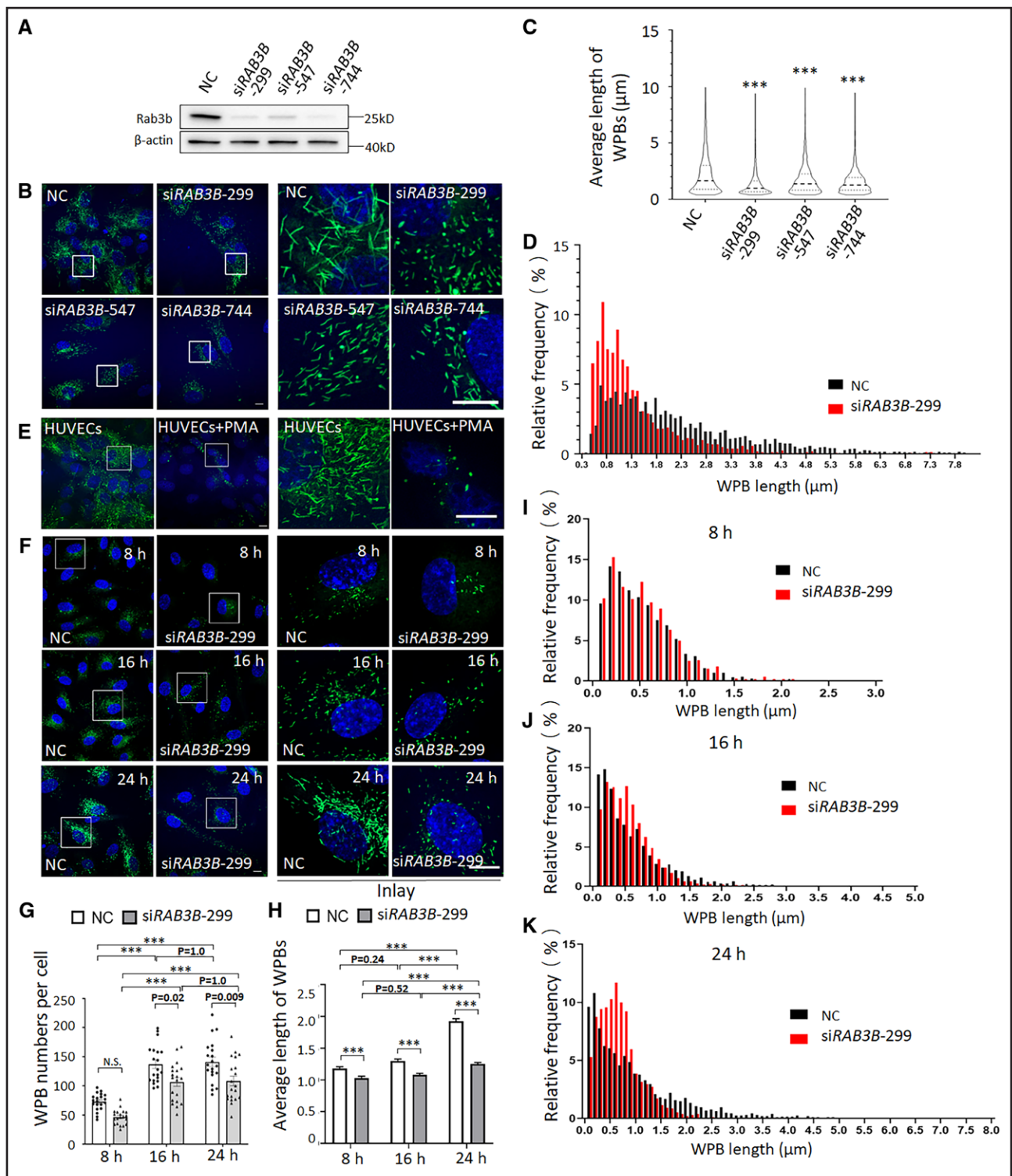
Figure 5. Rab3b deficiency affects Weibel-Palade body (WPB) morphology in human umbilical vein endothelial cells (HUVECs).
A, *RAB3B* was efficiently knocked down by 3 different siRNA (si*RAB3B*-299, -547, and -744) in HUVECs. The protein levels of Rab3b were detected by Western blotting. **B**, Immunofluorescence images were captured by the super-resolution mode of Airscan II after stained with an endogenous WPB marker vWF (green). Note, vWF-labeled WPBs in *RAB3B* knockdown are shorter than that in negative control (NC) cells. Three independent experiments were performed. Scale bars, 10 μm. **C**, Average length of WPBs was quantified. Three independent experiments were performed. We analyzed 2824 WPBs from NC cells, 2916 WPBs from si*RAB3B*-299 cells, 2670 WPBs from si*RAB3B*-547 cells and 1121WPBs from si*RAB3B*-744 cells. Data shown are mean±SEM, ***P<0.001, each knockdown group was compared with the control group by nonparametric Kruskal-Wallis test with Dunn post hoc. **D**, The distribution of WPB length was shifted to the shorter region in *RAB3B* knockdown cells. **E**, PMA stimulation cleared most of the existing WPBs. HUVECs were treated with or without 80 nmol/L PMA in growth medium for 30 minutes and then fixed immediately and stained with an endogenous (*Continued*)

suggesting that depletion of Rab3b disrupted normal WPB morphology, leading to a significant reduction of long rod-shaped WPBs in HUVECs. Considering that the HUVECs we obtained were derived from one individual, we repeated this experiment in another batch of HUVECs from another different individual (Figure S2).

It has been reported that mitochondria interact with melanosomes and participate in the biogenesis of melanosomes.[28] Likewise, endoplasmic reticulum and lipid droplet cross talk promotes lipid droplet growth and maturation.[43] As Rab3b deficiency dramatically reduced the size of WPBs, we then explored whether its depletion would disrupt nascent WPB growth by knocking down *RAB3B*. To track the morphological changes during newly formed WPB growth, we stimulated HUVEC cells with 80 nmol/L PMA treatment for 30 minutes to eliminate the interference of preexisting WPBs. After fixed at different time points, we then investigated which WPB morphological stage was affected by knocking down *RAB3B*. Majority of WPBs were emptied after PMA treatment, only a small number of vWF-labeled WPBs left around the perinuclear region (Figure 5E). From 8 to 16 or 24 hours after PMA washing out, the number of WPBs in both control cells and *RAB3B* knockdown cells was significantly increased. However, compared with the control cells, the number of WPBs in *RAB3B* knockdown cells was reduced (Figure 5F and 5G). After PMA washing out, the average length of vWF positive WPBs in control cells was significantly increased from 8 to 16 or 24 hours. However, in *RAB3B* knockdown cells, there was no significant increase in the average length of WPBs from 8 to 16 hours, and the average length of WPBs in *RAB3B* knockdown cells at each time point was significantly shorter than that in the control group (Figure 5F and 5H). From the length distribution graphs, the distribution of WPBs with different length in *RAB3B* knockdown cells was similar to that at 8 hours compared with the NC group (Figure 5I). However, at 24 hours, the proportion of WPB longer than 1.8 μm in NC group was more than that in *RAB3B* knockdown group, while more WPBs were distributed <1.8 μm in *RAB3B* knockdown group (Figure 5J and 5K). Taken together, these data suggest that Rab3b regulates the growth of newly formed WPBs in HUVECs.

Rab3b Deficiency Reduces Mitochondrion-WPB Contacts

We then investigated whether Rab3b functions in the interaction between mitochondria and WPBs. Our immunofluorescence analysis confirmed that endogenous Rab3b is mainly localized on vWF-labeled WPBs (Figure 6A). Exogenous expression of EGFP-Rab3b also showed the localization and enrichment of Rab3b on the WPBs (Figure 6B). Colocalization analysis with Mito-dsRed labeled mitochondria and vWF-labeled WPBs showed enrichment of Rab3b at inter-organellar contact sites (Figure 6C). The spatial location of Rab3b suggests that it may be involved in the interaction between mitochondria and WPB.

We used the algorithm that we developed as described in Figure 2A. The overlapped vWF-GFP and Mito-dsRed fluorescence marked the boundary between a WPB and a mitochondrion. This boundary might represent the mitochondria-WPBs contact. We then used the number and length of the boundary between Mito-dsRed and vWF as an indirect index to evaluate the mitochondria-WPBs contacts. To track mitochondrion-WPB contacts during WPB growth, *RAB3B*-knockdown and control HUVECs treated with 80 nmol/L PMA were fixed at different time points. Cells were stained with antibodies to endogenous TOMM20 (red) and vWF (green) and immunofluorescence images were captured (Figure 6D). From 8 to 16 hours in NC HUVECs, total contacts of each cell increased from 68.6 to 263.6 (Figure 6E), the contacts of a single WPB per cell increased from 1.6 to 2.9 (Figure 6F), the proportion of WPBs with contacts increased from 71.4% to 83.6% (Figure 6G), and the average contact length of each WPB increased from 0.69 to 1.33 μm (Figure 6H), indicating that the interaction between mitochondria and WPB at 16 hours was more active and frequent than that at 8 hours. However, in *RAB3B* knockdown cells, the above parameters did not increase obviously from 8 to 16 hours. Moreover, in *RAB3B* knockdown cells at 8 hours, the above parameters had no significant difference compared with NC cells. At 16 hours, the above parameters were all significantly reduced compared with control cells (Figure 6E through 6H). These results suggest that Rab3b functions after WPBs detach from the TGN

Figure 5 Continued. WPB marker vWF (green). Representative images show that the existing WPBs were mostly disappeared after PMA stimulation. Scale bars, 10 μm. **F**, NC and *RAB3B* knockdown HUVEC cells (si*RAB3B*-299) were treated with 80 nmol/L PMA for 30 minutes and chased for 8, 16, and 24 hours. Cells were fixed and stained with an endogenous WPB marker vWF (green). Representative images show that Rab3b deficiency in HUVECs affects the length of WPBs during the maturation process (8 hours–24 hours). Scale bars, 10 μm. **G**, Quantification of WPB numbers in NC and *RAB3B* knockdown cells at 8, 16, and 24 hours. Three independent experiments were performed. Data shown are mean±SEM, n=20 cells, ***$P<0.001$ by 2-way ANOVA with Tukey post hoc. **H**, Quantification of length of WPBs in NC and *RAB3B* knockdown cells at 8, 16, and 24 hours. Three independent experiments were performed. Data shown are mean±SEM. WPB numbers in NC and si*RAB3B*-299 cells at 8 hours: 1209 vs 687; at 16 hours: 1393 vs 987; at 24 hours: 1587 vs 1611. ***$P<0.001$ by nonparametric Kruskal-Wallis test with Dunn post hoc. **I** through **K**, The distribution of WPB length in NC and si*RAB3B*-299 cells at 8, 16, and 24 hours was shown.
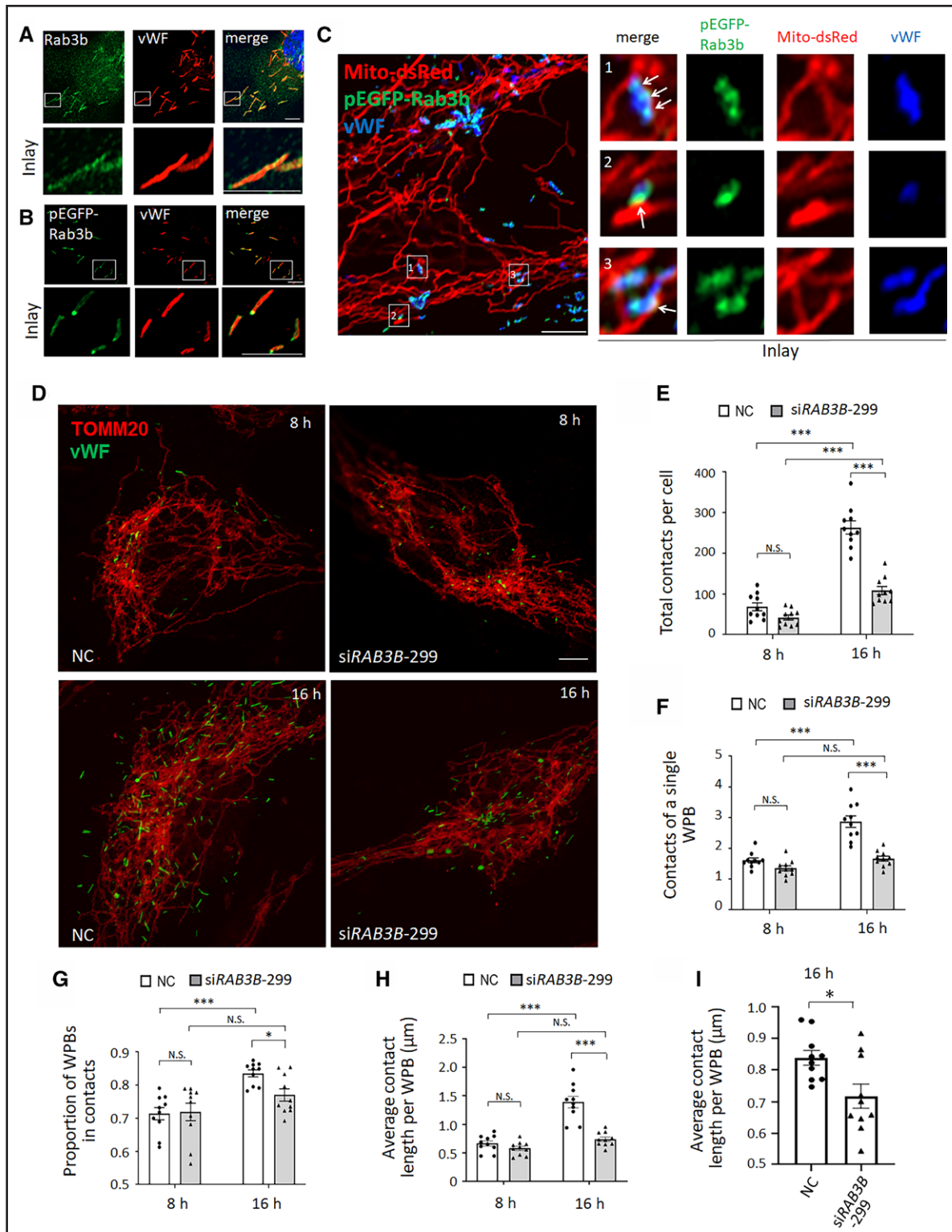
BASIC SCIENCES - VB

Figure 6. Decreased mitochondrion-Weibel-Palade body (WPB) contacts in *RAB3B* knockdown cells.
A, Fixed human umbilical vein endothelial cells (HUVECs) were stained for immunofluorescence with antibodies to endogenous Rab3b (green) and vWF (von Willebrand factor; red). Merged super-resolution images show that Rab3b distributed in clusters around WPBs. Scale bars, 5 μm. **B**, HUVECs transfected with EGFP-Rab3b were stained for immunofluorescence with an antibody to endogenous vWF (red). Merged super-resolution images show that EGFP-Rab3b (green) is localized at the end or in the middle of WPBs. Scale bars, 5 μm. **C**, HUVECs transfected with EGFP-Rab3b (green) and Mito-dsRed (red) were stained for immunofluorescence with endogenous vWF (blue). Note that some EGFP-Rab3b clusters are present at mitochondrion-WPB contact sites. Scale bar, 2 μm. **D**, *RAB3B* was knocked down by si*RAB3B*-299 in HUVECs and cells were treated with 80 nmol/L PMA for 30 minutes and chased for 8 and 16 hours. (*Continued*)

by affecting further elongation and maturation, which occur between 8 and 16 hours.

As the observed reduction in WPB length was seen when *RAB3B* was knocked down at the 16-hour time point of WPB biogenesis, we further conducted a statistical analysis of the contact length between WPBs and mitochondria for all newly generated WPBs with a perimeter of <6 µm. Our results showed a significant reduction in the average contact length per WPB in the *RAB3B* knockdown group compared with the control group within the same perimeter range of WPBs (Figure 6I). Taken together, Rab3b possibly play a role in the formation of the mitochondrion-WPB inter-organellar connections during WPB maturation.

Disruption of Mitochondrion-WPB Contacts by Rab3b Deficiency Affects vWF Multimers Secretion of WPBs

The physiological function of WPB is mainly reflected in the release of vWF multimers to participate in coagulation after stimulation. Since disruption of mitochondrion-WPB contacts by Rab3b deficiency affects WPB maturation, we next examined vWF multimers secretion in *RAB3B* knockdown HUVECs to analyze whether WPB physiological function is affected. The NC and the knockdown group were stimulated by PMA for 30 minutes, and the supernatants were collected to detect vWF multimers secreted out of the cells. Our results showed that the regulatory secretion of vWF multimers upon stimulation was significantly increased in control cells. However, although the secretion of vWF multimers was also seen after stimulation in *RAB3B* knockdown cells, the secreted vWF multimers was significantly reduced compared with control group, relative to the same amount of cell proteins (Figure 7). This suggests that the effect of mitochondrion-WPB contacts on WPB maturation likewise affects secretion, an important physiological function of WPBs.

DISCUSSION

WPB is a unique secretory organelle in vascular endothelial cells. Various types of molecular machinery regulate the formation and maturation of WPBs.[18,19] In this study, we have demonstrated the interaction between mitochondria and WPB physically and functionally. We

showed that WPBs directly interacted with mitochondria within tens of nanometers by using high resolution SIM and electron microscopy. By time lapse analysis, fluorescently labeled mitochondria and WPBs were often found coupled in close vicinity of each other in organelle dynamics. We propose that the biological function of mitochondrion-WPB contacts is related to the development of nascent WPBs, because depletion of Rab3b, a Rab GTPase of WPBs enriched at interaction sites, reduced contact between WPB and mitochondria,and impeded the growth of newly formed WPBs, thus affected the secretion of vWF multimers.

Our results showed that the size of WPB in Rab3b-deficient cells was shortened. Previous studies reported that Rab3b deficiency did not affect secretion in HUVECs.[44] Their experiment and calculation methods are different from ours. They used ELISA to quantify vWF, and vWF secretion was calculated by dividing the total vWF content, which contains both secreted and intracellular vWF. This secreted vWF may represent both basal/unstimulated release and regulated secretion. Their experiments showed that Rab3b may not affect the secretion ability of individual WPBs. Our calculation method was to quantify the amount of secreted vWF by dividing the total β-actin content of the cells. Our results showed that for the same number of cells, the total amount of vWF multimers secreted by *RAB3B* knockdown cells was decreased. The amount of vWF multimers in our calculation mostly represents the regulated secretion of vWF from mature WPBs. However, we observed slightly increased secretion of vWF multimers in *RAB3B* knockdown cells upon stimulation although it was not statistically significant (Figure 7). It is likely that these WPBs with abnormal morphology caused by Rab3b deficiency may be subject to secretion, but Rab3b deficiency may affect the amount of high molecular weight vWF multimers stored within WPBs, resulting in reduced regulated secretion of WPB. A similar role of phosphatidylinositol-4 kinases (PI4IIα and PI4IIβ) has also been observed, WPB size reduced in PI4KII-deficient cells, but the secretion capacity remains unchanged.[45] In contrast, Rab27 was previously shown to be located on mature WPB[46] and involved in WPB secretion.[24] In our results, Rab27a depletion led to a very minor effect on WPB morphology (maturation). By tracing the maturation process of WPB, we observed that the maturation of WPB was impaired in Rab3b deficient cells, suggesting that Rab3b promotes maturation of

Figure 6 Continued. Then, fixed HUVECs were stained with antibodies to endogenous TOMM20 (red) and vWF (green). Scale bars, 5 µm. **E** through **G**, Quantification of the total contacts of each cell (**E**), the contacts of a single WPB (**F**), and the proportion of contacted WPB (**G**) in negative control (NC) and *RAB3B* knockdown cells. Data shown are mean±SEM, n=10 cells, ***P*<0.001 by 2-way ANOVA with Tukey post hoc. **H**, Quantification of the contact length of each WPB per cell in NC and *RAB3B* knockdown cells. Data shown are mean±SEM, n=10 cells, ***P*<0.001 by 2-way ANOVA with Tukey post hoc. **I**, The contact length between WPBs and mitochondria for all newly generated WPBs with a perimeter of <6 µm at the 16-hour time point was quantified in NC and *RAB3B* knockdown cells. We selected the threshold of 6 µm perimeter for the reason that at 8 hours, nearly all WPBs had perimeters <6 µm, while at 16 hours, the NC group exhibited many longer WPBs, whereas the Rab3b knockdown group had almost no WPBs >6 µm. Data shown are mean±SEM, n=10 cells, *P*=0.014 by unpaired 2-tailed *t* test.
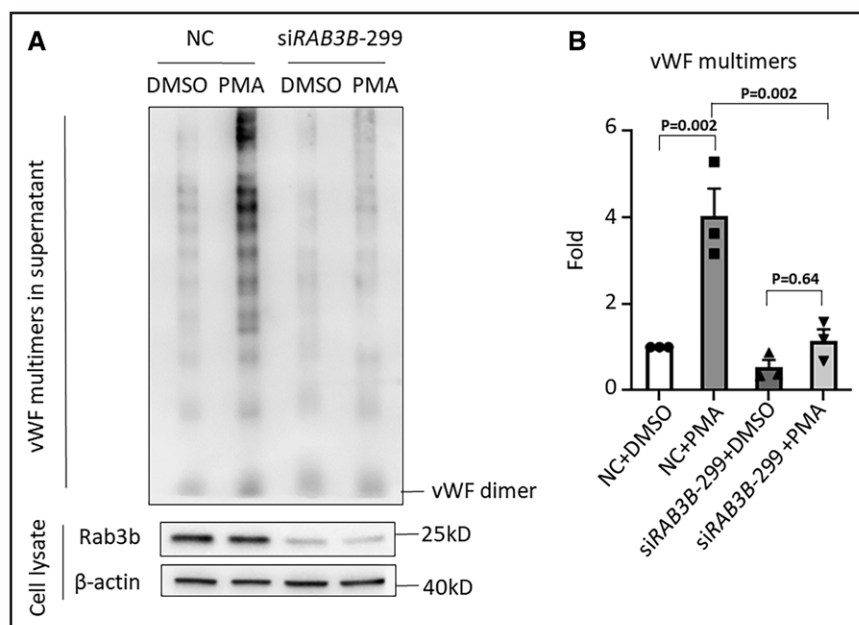
Figure 7. Rab3b deficiency compromises vWF (von Willebrand factor) secretion in human umbilical vein endothelial cells (HUVECs).
A, *RAB3B* was knocked down by siRNA in HUVECs. After 72 hours, cells were treated with DMSO or 80 nmol/L PMA in 200 μL growth medium at 37 °C for 30 minutes, and the supernatant and cell lysate of each group were collected. Western blotting analysis of vWF multimers secretion in supernatant, and Rab3b and β-actin in cell lysates were performed. The approximate molecular weight of vWF dimer is 450 kD. Bands were analyzed using National Institutes of Health Image J software. **B**, The quantification of supernatant vWF multimers was carried out based on the normalization of β-actin of the total cell lysates in each group. Three independent experiments were performed. Data shown are mean±SEM, n=3, *P* values by 1-way ANOVA with Tukey post hoc.

nascent WPBs. It is possible that the distinct localization of Rab3b and Rab27 may control WPB maturation and secretion, respectively. In summary, Rab3b may not affect the secretion ability but affect the maturation stage of WPBs.

It is intriguing to reveal the interaction partner of Rab3b on the mitochondria. Holthenrich et al identified several WPB-associated factors via a proximity proteomics approach employing the peroxidase APEX2 coupled with 2 known WPB-associated proteins: Rab3b and Rab27a. Among the WPB-associated proteins they identified, there were some mitochondrial localized proteins, such as TOMM70, PTRH2, CYB5R3, and ACSL4, which may be candidate Rab3b interacting counterparts on mitochondria.[47] Further investigation is required for the identification of the interaction machinery.

The rod-like structure of WPB has been reported to form at TGN[15,48]; however, it is unclear whether immature WPB continues to elongate after dissociation from TGN. Our results showed that from 8 to 24 hours after PMA stimulation, most WPBs had left the perinuclear region. The rod-shaped structure of WPBs extended from about 1.18 μm at 8 hours to about 1.93 μm at 24 hours (Figure 5H). Moreover, in our experiments, the average length of WPB in cells without PMA stimulation was generally about 2 μm (Figure 5D). These suggest that WPBs undergo elongation during maturation after exit from TGN. Rab3b may regulate the growth of immature WPB by promoting the cross talk between WPB and mitochondria.

The possible physiological function(s) of the mitochondrion-WPB contacts is to be defined. An attractive hypothesis is that mitochondrion and WPB form a local channel at the contact site to facilitate the transfer of small molecules from mitochondria for WPB biogenesis.

Mitochondria are the primary site for ATP synthesis, we noticed that treating cells with oligomycin A and depletion of *NDUFS1, SLC25A4* or *SLC25A5*, which inhibits ATP synthesis, led to a decreased number of long rod-shaped WPBs, suggesting that mitochondria may provide ATP for WPB maturation. Similarly, it was found that mitochondria may regulate the biogenesis of melanosomes by transporting ATP to melanosomes (another type of lysosome-related organelle).[28] It is also possible that not only ATP but also other small molecules might be delivered to WPBs from mitochondria. Our previous study has shown that NCKX5, a Na$^+$/Ca^{2+} exchanger located on mitochondria, mediates Ca^{2+} transfer from mitochondria to melanosomes directly to regulate pigment production.[29] Here, we found that knockdown of *SLC8A3*, a modulator of mitochondrial calcium efflux,[40,41] significantly affected WPB size in HUVECs. Thus, mitochondrion-WPB contacts might function as platforms for inter-organelle calcium flux between mitochondria and WPBs to regulate WPB maturation and function. We also observed reduced size of WPBs by disrupting mitochondrial fusion and fission in *MFN2* and *FIS1* knocking down cells. Mitochondria are highly dynamic, which may serve as a supporting structure to modulate WPB homeostasis.

This study reveals a complex pattern of mitochondrion-WPB interactions using time-lapse live-cell imaging. We found that different contact events exist based on their motility characteristics, maturation stage of WPBs, location, and function. These interactions may have profound effects on the dynamics of both organelles. The nature and underlying molecular mechanism of these various forms of interaction warrant further investigations. Altered mitochondrion-WPB interaction may affect the biogenesis and homeostasis of both

organelles, providing insights into the underlying mechanism of organelle pathology.

REFERENCES

1. Huizing M, Helip-Wooley A, Westbroek W, Gunay-Aygun M, Gahl WA. Disorders of lysosome-related organelle biogenesis: clinical and molecular genetics. *Annu Rev Genomics Hum Genet*. 2008;9:359–386. doi: 10.1146/annurev.genom.9.081307.164303

2. Li W, Hao CJ, Hao ZH, Ma J, Wang QC, Yuan YF, Gong JJ, Chen YY, Yu JY, Wei AH. New insights into the pathogenesis of Hermansky-Pudlak syndrome. *Pigment Cell Melanoma Res*. 2022;35:290–302. doi: 10.1111/pcmr.13030

3. Cutler DF. Introduction: lysosome-related organelles. *Semin Cell Dev Biol*. 2002;13:261–262. doi: 10.1016/s1084952102000054x

4. Metcalf DJ, Nightingale TD, Zenner HL, Lui-Roberts WW, Cutler DF. Formation and function of Weibel-Palade bodies. *J Cell Sci*. 2008;121:19–27. doi: 10.1242/jcs.03494

5. Huang RH, Wang Y, Roth R, Yu X, Purvis AR, Heuser JE, Egelman EH, Sadler JE. Assembly of Weibel-Palade body-like tubules from N-terminal domains of von Willebrand factor. *Proc Natl Acad Sci U S A*. 2008;105:482–487. doi: 10.1073/pnas.0710079105

6. Fiedler U, Scharpfenecker M, Koidl S, Hegen A, Grunow V, Schmidt JM, Kriz W, Thurston G, Augustin HG. The Tie-2 ligand angiopoietin-2 is stored in and rapidly released upon stimulation from endothelial cell Weibel-Palade bodies. *Blood*. 2004;103:4150–4156. doi: 10.1182/blood-2003-10-3685

7. Rosnoblet C, Ribba AS, Wollheim CB, Kruithof EK, Vischer UM. Regulated von Willebrand factor (vWf) secretion is restored by pro-vWf expression in a transfectable endothelial cell line. *Biochim Biophys Acta*. 2000;1495:112–119. doi: 10.1016/s0167-4889(99)00150-0

8. Hol J, Küchler AM, Johansen FE, Dalhus B, Haraldsen G, Oynebråten I. Molecular requirements for sorting of the chemokine interleukin-8/CXCL8 to endothelial Weibel-Palade bodies. *J Biol Chem*. 2009;284:23532–23539. doi: 10.1074/jbc.M900874200

9. Valentijn KM, Sadler JE, Valentijn JA, Voorberg J, Eikenboom J. Functional architecture of Weibel-Palade bodies. *Blood*. 2011;117:5033–5043. doi: 10.1182/blood-2010-09-267492

10. Sadler JE, Mannucci PM, Berntorp E, Bochkov N, Boulyjenkov V, Ginsburg D, Meyer D, Peake I, Rodeghiero F, Srivastava A. Impact, diagnosis and treatment of von Willebrand disease. *Thromb Haemost*. 2000;84:160–174.

11. Levy GG, Nichols WC, Lian EC, Foroud T, McClintick JN, McGee BM, Yang AY, Siemieniak DR, Stark KR, Gruppo R, et al. Mutations in a member of the ADAMTS gene family cause thrombotic thrombocytopenic purpura. *Nature*. 2001;413:488–494. doi: 10.1038/35097008

12. van Galen KPM, Tuinenburg A, Smeets EM, Schutgens RE. Von Willebrand factor deficiency and atherosclerosis. *Blood Rev*. 2012;26:189–196. doi: 10.1016/j.blre.2012.05.002

13. Wagner DD, Olmsted JB, Marder VJ. Immunolocalization of von Willebrand protein in Weibel-Palade bodies of human endothelial cells. *J Cell Biol*. 1982;95:355–360. doi: 10.1083/jcb.95.1.355

14. Zhou YF, Eng ET, Nishida N, Lu C, Walz T, Springer TA. A pH-regulated dimeric bouquet in the structure of von Willebrand factor. *EMBO J*. 2011;30:4098–4111. doi: 10.1038/emboj.2011.297

15. Ferraro F, Kriston-Vizi J, Metcalf DJ, Martin-Martin B, Freeman J, Burden JJ, Westmoreland D, Dyer CE, Knight AE, Ketteler R, et al. A two-tier Golgi-based control of organelle size underpins the functional plasticity of endothelial cells. *Dev Cell*. 2014;29:292–304. doi: 10.1016/j.devcel.2014.03.021

16. Zenner HL, Collinson LM, Michaux G, Cutler DF. High-pressure freezing provides insights into Weibel-Palade body biogenesis. *J Cell Sci*. 2007;120:2117–2125. doi: 10.1242/jcs.007781

17. Ma J, Zhang Z, Yang L, Kriston-Vizi J, Cutler DF, Li W. BLOC-2 subunit HPS6 deficiency affects the tubulation and secretion of von Willebrand factor from mouse endothelial cells. *J Genet Genomics*. 2016;43:686–693. doi: 10.1016/j.jgg.2016.09.007

18. Naß J, Terglane J, Gerke V. Weibel Palade bodies: unique secretory organelles of endothelial cells that control blood vessel homeostasis. *Front Cell Dev Biol*. 2021;9:813995. doi: 10.3389/fcell.2021.813995

19. Mourik M, Eikenboom J. Lifecycle of Weibel-Palade bodies. *Hamostaseologie*. 2017;37:13–24. doi: 10.5482/HAMO-16-07-0021

20. Terglane J, Menche D, Gerke V. Acidification of endothelial Weibel-Palade bodies is mediated by the vacuolar-type H+-ATPase. *PLoS One*. 2022;17:e0270299. doi: 10.1371/journal.pone.0270299

21. Harrison-Lavoie KJ, Michaux G, Hewlett L Kaur J, Hannah MJ, Lui-Roberts WW, Norman KE, Cutler DF. P-selectin and CD63 use different mechanisms for delivery to Weibel-Palade bodies. *Traffic*. 2006;7:647–662. doi: 10.1111/j.1600-0854.2006.00415.x

22. Lu J, Ma J, Hao Z, Li W. HPS6 Regulates the biogenesis of Weibel-Palade body in endothelial cells through trafficking v-ATPase to its limiting membrane. *Front Cell Dev Biol*. 2022;9:743124. doi: 10.3389/fcell.2021.743124

23. Yamazaki Y, Eura Y, Kokame K. V-ATPase V0a1 promotes Weibel-Palade body biogenesis through the regulation of membrane fission. *Elife*. 2021;10:e71526. doi: 10.7554/eLife.71526

24. Bierings R, Hellen N, Kiskin N, Knipe L, Fonseca AV, Patel B, Meli A, Rose M, Hannah MJ, Carter T. The interplay between the Rab27A effectors Slp4-a and MyRIP controls hormone-evoked Weibel-Palade body exocytosis. *Blood*. 2012;120:2757–2767. doi: 10.1182/blood-2012-05-429936

25. Szymański J, Janikiewicz J, Michalska B, Patalas-Krawczyk P, Perrone M, Ziółkowski W, Duszyński J, Pinton P, Dobrzyń A, Więckowski MR. Interaction of mitochondria with the endoplasmic reticulum and plasma membrane in calcium homeostasis, lipid trafficking and mitochondrial structure. *Int J Mol Sci*. 2017;18:1576. doi: 10.3390/ijms18071576

26. Wang J, Fang N, Xiong J, Du Y, Cao Y, Ji WK. An ESCRT-dependent step in fatty acid transfer from lipid droplets to mitochondria through VPS13D-TSG101 interactions. *Nat Commun*. 2021;12:1252. doi: 10.1038/s41467-021-21525-5

27. Wong YC, Ysselstein D, Krainc D. Mitochondria-lysosome contacts regulate mitochondrial fission via RAB7 GTP hydrolysis. *Nature*. 2018;554:382–386. doi: 10.1038/nature25486

28. Daniele T, Hurbain I, Vago R, Casari G, Raposo G, Tacchetti C, Schiaffino MV. Mitochondria and melanosomes establish physical contacts modulated by Mfn2 and involved in organelle biogenesis. *Curr Biol*. 2014;24:393–403. doi: 10.1016/j.cub.2014.01.007

29. Zhang Z, Gong J, Sviderskaya EV, Wei A, Li W. Mitochondrial NCKX5 regulates melanosomal biogenesis and pigment production. *J Cell Sci*. 2019;132:jcs232009. doi: 10.1242/jcs.232009

30. Huang X, Fan J, Li L, Liu H, Wu R, Wu Y, Wei L, Mao H, Lal A, Xi P, et al. Fast, long-term, super-resolution imaging with Hessian structured illumination microscopy. *Nat Biotechnol.* 2018;36:451–459. doi: 10.1038/nbt.4115

31. Liu L, Yang S, Liu Y, Li X, Hu J, Xiao L, Xu T. DeepContact: high-throughput quantification of membrane contact sites based on electron microscopy imaging. *J Cell Biol.* 2022;221:e202106190. doi: 10.1083/jcb.202106190

32. Ronneberger O, Fischer P, Brox T. U-Net: Convolutional networks for biomedical image segmentation. *Medical Image Computing and Computer-Assisted Intervention-MICCAI.* Cham: Springer International Publishing; 2015:234–241. https://doi.org/10.48550/arXiv.1505.04597

33. Tinevez JY, Perry N, Schindelin J, Hoopes GM, Reynolds GD, Laplantine E, Bednarek SY, Shorte SL, Eliceiri KW. TrackMate: an open and extensible platform for single-particle tracking. *Methods.* 2017;115:80–90. doi: 10.1016/j.ymeth.2016.09.016

34. Livak KJ, Schmittgen TD. Analysis of relative gene expression data using real-time quantitative PCR and the 2(-Delta Delta C(T)) Method. *Methods.* 2001;25:402–408. doi: 10.1006/meth.2001.1262

35. Dorn GW 2nd. Mitofusins as mitochondrial anchors and tethers. *J Mol Cell Cardiol.* 2020;142:146–153. doi: 10.1016/j.yjmcc.2020.04.016

36. Zhang Z, Liu L, Wu S, Xing D. Drp1, Mff, Fis1, and MiD51 are coordinated to mediate mitochondrial fission during UV irradiation-induced apoptosis. *FASEB J.* 2016;30:466–476. doi: 10.1096/fj.15-274258

37. Fiore C, Trézéguet V, Le Saux A, Roux P, Schwimmer C, Dianoux AC, Noel F, Lauquin GJ, Brandolin G, Vignais PV. The mitochondrial ADP/ATP carrier: structural, physiological and pathological aspects. *Biochimie.* 1998;80:137–150. doi: 10.1016/s0300-9084(98)80020-5

38. Klingenberg M. The ADP and ATP transport in mitochondria and its carrier. *Biochim Biophys Acta.* 2008;1778:1978–2021. doi: 10.1016/j.bbamem.2008.04.011

39. Cho J, Seo J, Lim CH, Yang L, Shiratsuchi T, Lee M-H, Chowdhury RR, Kasahara H, Kim J-S, Oh SP, et al. Mitochondrial ATP transporter Ant2 depletion impairs erythropoiesis and B lymphopoiesis. *Cell Death Differ.* 2015;22:1437–1450. doi: 10.1038/cdd.2014.230

40. Scorziello A, Savoia C, Sisalli MJ, Adornetto A, Secondo A, Boscia F, Esposito A, Polishchuk EV, Polishchuk RS, Molinaro P, et al. NCX3 regulates mitochondrial Ca(2+) handling through the AKAP121-anchored signaling complex and prevents hypoxia-induced neuronal death. *J Cell Sci.* 2013;126:5566–5577. doi: 10.1242/jcs.129668

41. Sisalli MJ, Feliciello A, Della Notte S, Di Martino R, Borzacchiello D, Annunziato L, Scorziello A. Nuclear-encoded NCX3 and AKAP121: two novel modulators of mitochondrial calcium efflux in normoxic and hypoxic neurons. *Cell Calcium.* 2020;87:102193. doi: 10.1016/j.ceca.2020.102193

42. Luongo TS, Lambert JP, Gross P, Nwokedi M, Lombardi AA, Shanmughapriya S, Carpenter AC, Kolmetzky D, Gao E, van Berlo JH, et al. The mitochondrial Na(+)/Ca(2+) exchanger is essential for Ca(2+) homeostasis and viability. *Nature.* 2017;545:93–97. doi: 10.1038/nature22082

43. Xu D, Li Y, Wu L, Li Y, Zhao D, Yu J, Huang T, Ferguson C, Parton RG, Yang H, et al. Rab18 promotes lipid droplet (LD) growth by tethering the ER to LDs through SNARE and NRZ interactions. *J Cell Biol.* 2018;217:975–995. doi: 10.1083/jcb.201704184

44. Zografou S, Basagiannis D, Papafotika A, Shirakawa R, Horiuchi H, Auerbach D, Fukuda M, Christoforidis S. A complete Rab screening reveals novel insights in Weibel-Palade body exocytosis. *J Cell Sci.* 2012;125:4780–4790. doi: 10.1242/jcs.104174

45. Lopes da Silva M, O'Connor MN, Kriston-Vizi J, White IJ, Al-Shawi R, Simons JP, Mössinger J, Haucke V, Cutler DF. Type II PI4-kinases control Weibel-Palade body biogenesis and von Willebrand factor structure in human endothelial cells. *J Cell Sci.* 2016;129:2096–2105. doi: 10.1242/jcs.187864

46. Hannah MJ, Hume AN, Arribas M, Williams R, Hewlett LJ, Seabra MC, Cutler DF. Weibel-Palade bodies recruit Rab27 by a content-driven, maturation-dependent mechanism that is independent of cell type. *J Cell Sci.* 2003;116:3939–3948. doi: 10.1242/jcs.00711

47. Holthenrich A, Drexler HCA, Chehab T, Naß J, Gerke V. Proximity proteomics of endothelial Weibel-Palade bodies identifies novel regulator of von Willebrand factor secretion. *Blood.* 2019;134:979–982. doi: 10.1182/blood.2019000786

48. Mourik MJ, Faas FG, Zimmermann H, Voorberg J, Koster AJ, Eikenboom J. Content delivery to newly forming Weibel-Palade bodies is facilitated by multiple connections with the Golgi apparatus. *Blood.* 2015;125:3509–3516. doi: 10.1182/blood-2014-10-608596